J|A|C|S
ARTICLES

Mixed Low-Dimensional Nanomaterial: 2D Ultranarrow MoS_2 Inorganic Nanoribbons Encapsulated in Quasi-1D Carbon Nanotubes

Zhiyong Wang,[†,#] Hong Li,[‡,#] Zheng Liu,[§,#] Zujin Shi,[*,†] Jing Lu,[*,‡] Kazu Suenaga,[*,§] Soon-Kil Joung,[§] Toshiya Okazaki,[§] Zhennan Gu,[†] Jing Zhou,[‡] Zhengxiang Gao,[‡] Guangping Li,[||] Stefano Sanvito,[⊥] Enge Wang,[‡] and Sumio Iijima[§]

Beijing National Laboratory for Molecular Sciences, State Key Lab of Rare Earth Materials Chemistry and Applications, College of Chemistry and Molecular Engineering, Peking University, Beijing 100871, P. R. China, State Key Laboratory of Mesoscopic Physics and Department of Physics, Peking University, Beijing 100871, P. R. China, Nanotube Research Center, National Institute of Advanced Industrial Science and Technology (AIST), Tsukuba 305-8565, Japan, SICAS Center, Lee Hall, SUNY Oneonta, Oneonta, New York 13820, and School of Physics and CRANN, Trinity College, Dublin 2, Ireland

Received July 1, 2010; E-mail: zjshi@pku.edu.cn; jinglu@pku.edu.cn; suenaga-kazu@aist.go.jp

Abstract: Quasi-one-dimensional nanotubes and two-dimensional nanoribbons are two fundamental forms of nanostructures, and integrating them into a novel mixed low-dimensional nanomaterial is fascinating and challenging. We have synthesized a stable mixed low-dimensional nanomaterial consisting of MoS_2 inorganic nanoribbons encapsulated in carbon nanotubes (which we call nanoburritos). This route can be extended to the synthesis of nanoburritos composed of other ultranarrow transition-metal chalcogenide nanoribbons and carbon nanotubes. The widths of previously synthesized MoS_2 ribbons are greater than 50 nm, while the encapsulated MoS_2 nanoribbons have uniform widths down to 1−4 nm and layer numbers down to 1−3, depending on the nanotube diameter. The edges of the MoS_2 nanoribbons have been identified as zigzag-shaped using both high-resolution transmission electron microscopy and density functional theory calculations.

Introduction

Novel properties may arise when the size of a material is decreased to the nanoscale and the dimension is lowered because of quantum confinement effects and edge effects. Carbon nanotubes (CNTs) constitute a quasi-one-dimensional (quasi-1D) nanomaterial and have been extensively studied since their discovery in 1991 by Iijima.[1] Perhaps equally important is the discovery of inorganic tungsten disulfide (WS_2) nanotubes by Tenne in 1992,[2] which established a new paradigm in the chemistry of nanomaterials and led to the birth of a new field of inorganic chemistry. Later, fullerene-like MoS_2 clusters[3] and triangular-shaped single-layer MoS_2 nanoclusters[4−6] were synthesized. Although bulk MoS_2 is a nonmagnetic semiconductor, triangular-shaped single-layer MoS_2 nanoclusters have been reported to have metallic edges on the basis of scanning tunneling spectroscopy (STM) observations and density functional theory (DFT) calculations,[4,7] and magnetism has been observed in weakly coupled lithium-doped MoS_2 nanotubes[8] and triangular-shaped nanosheet-like MoS_2 films.[9] The potential application areas of MoS_2 nanostructures range from nanotribology,[10] photocatalysts,[11] hydrogen production,[12] and solar cells[13] to the active sites of some enzymes.[14,15]

[†] Beijing National Laboratory for Molecular Sciences and State Key Lab of Rare Earth Materials Chemistry and Applications, Peking University.

[‡] State Key Laboratory of Mesoscopic Physics and Department of Physics, Peking University.

[§] National Institute of Advanced Industrial Science and Technology.

[||] SUNY Oneonta.

[⊥] Trinity College Dublin.

[#] These authors contributed equally.

(1) Iijima, S. *Nature* **1991**, *354*, 56–58.

(2) Tenne, R.; Margulis, L.; Genut, M.; Hodes, G. *Nature* **1992**, *360*, 444–446.

(3) Margulis, L.; Salitra, G.; Tenne, R.; Talianker, M. *Nature* **1993**, *365*, 113–114.

(4) Bollinger, M. V.; Lauritsen, J. V.; Jacobsen, K. W.; Norskov, J. K.; Helveg, S.; Besenbacher, F. *Phys. Rev. Lett.* **2001**, *87*, 196803.

(5) Helveg, S.; Lauritsen, J. V.; Laegsgaard, E.; Stensgaard, I.; Norskov, J. K.; Clausen, B. S.; Topsoe, H.; Besenbacher, F. *Phys. Rev. Lett.* **2000**, *84*, 951–954.

(6) Lauritsen, J. V.; Kibsgaard, J.; Helveg, S.; Topsoe, H.; Clausen, B. S.; Laegsgaard, E.; Besenbacher, F. *Nat. Nanotechnol.* **2007**, *2*, 53–58.

(7) Bollinger, M. V.; Jacobsen, K. W.; Norskov, J. K. *Phys. Rev. B* **2003**, *67*, 085410.

(8) Jaglicic, Z.; Jeromen, A.; Trontelj, Z.; Mihailovic, D.; Arcon, D.; Remskar, M.; Mrzel, A.; Dominko, R.; Gaberscek, M.; Martinez-Agudo, J. M.; Gomez-Garcia, C. J.; Coronado, E. *Polyhedron* **2003**, *22*, 2293–2295.

(9) Zhang, J.; Soon, J. M.; Loh, K. P.; Yin, J. H.; Ding, J.; Sullivian, M. B.; Wu, P. *Nano Lett.* **2007**, *7*, 2370–2376.

(10) Rapoport, L.; Bilik, Y.; Feldman, Y.; Homyonfer, M.; Cohen, S. R.; Tenne, R. *Nature* **1997**, *387*, 791–793.

(11) Wilcoxon, J. P.; Thurston, T. R.; Martin, J. E. *Nanostruct. Mater.* **1999**, *12*, 993–997.

(12) Hinnemann, B.; Moses, P. G.; Bonde, J.; Jorgensen, K. P.; Nielsen, J. H.; Horch, S.; Chorkendorff, I.; Norskov, J. K. *J. Am. Chem. Soc.* **2005**, *127*, 5308–5309.

(13) Kline, G.; Kam, K. K.; Ziegler, R.; Parkinson, B. A. *Sol. Energy Mater.* **1982**, *6*, 337–350.

(14) Chan, M. K.; Kim, J. S.; Rees, D. C. *Science* **1993**, *260*, 792–794.

10.1021/ja1058026

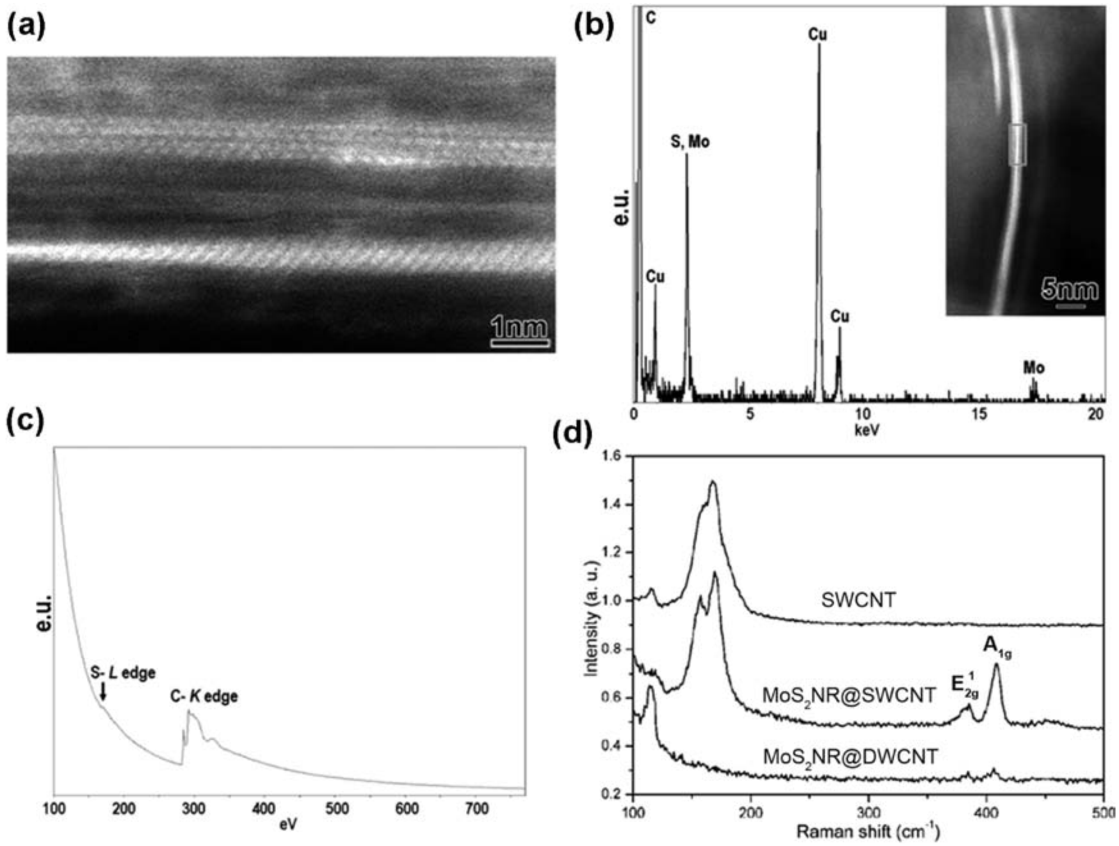

Figure 1. (a) Annular dark-field image of single-layer MoS$_2$NRs. (b) Micro-EDX and (c) micro-EELS signals obtained from the area denoted by the rectangle in the annular dark-field image (inset). (d) Raman spectra of SWCNTs, MoS$_2$NR@SWCNTs, and MoS$_2$NR@DWCNTs. The $E_2^1{}_g$ and A_{1g} modes characteristic of MoS$_2$ can be seen. The Raman signals in the 100−200 cm^{-1} range correspond to the CNT radial breathing mode.

Nanoribbon materials are ones having a restricted two-dimensional (2D) form in one direction, and they have become the focus of substantial recent research, partially because of the rise of graphene nanoribbons (GNRs).[16−19] Ultranarrow few-layer and even single-layer GNRs with widths of 10−20 nm[17] or smaller[19,20] have been synthesized very recently. Distinct from conducting graphene, GNRs less than 10 nm in width are always semiconducting.[19] In contrast, currently synthesized MoS$_2$ ribbons have widths of >50 nm and layer numbers greater than 5, and their edges are often rough.[21−23] Several interesting questions arise: (1) Is it possible to fabricate few-layer or even single-layer ultranarrow MoS$_2$ nanoribbons (MoS$_2$NRs) with uniform widths down to the exciton Bohr radius of MoS$_2$ (4 nm)? (2) If it exists, is this synthesis method extendable to other inorganic nanoribbons? (3) What is the edge structure of MoS$_2$NRs? (4) Now that zero-dimensional (0D) C$_{60}$ can be encapsulated inside CNTs to form a 0D-quasi-1D mixed low-dimensional nanomaterial ("nanopeapods"),[24] can 2D nanoribbons and quasi-1D nanotubes be integrated into a novel 2D-quasi-1D mixed low-dimensional nanomaterial?

In this article, we report the synthesis of a stable 2D-quasi-1D mixed low-dimensional nanomaterial consisting of ultranarrow MoS$_2$ inorganic nanoribbons inside single-walled carbon nanotubes (SWCNTs) (labeled as MoS$_2$NR@SWCNTs) and double-walled carbon nanotubes (DWCNTs) (labeled as MoS$_2$NR@DWCNTs); we call these structures "nanoburritos". This route can be extended to the synthesis of nanoburritos composed of other ultranarrow transition-metal chalcogenide nanoribbons (e.g., WS$_2$, SnS$_2$, VS$_2$, and TiS$_2$) and CNTs. The encapsulated MoS$_2$ nanoribbons have uniform widths down to 1−4 nm and layer numbers down to 1−3, and their edges have been identified as having a zigzag structure.

Experimental Section

SWCNTs and DWCNTs were produced by the arc-discharge method.[25,26] First, 5 mg of CNTs were dispersed in 10 mL of a saturated aqueous solution of H$_3$PMo$_{12}$O$_{40}$ by sonication for 1 h followed by refluxing for 2 h. H$_3$PMo$_{12}$O$_{40}$ was encapsulated into the CNTs during the sonication and reflux procedure. Next, the

---

(15) Hinnemann, B.; Norskov, J. K. *J. Am. Chem. Soc.* **2004**, *126*, 3920–3927.
(16) Geim, A. K.; Novoselov, K. S. *Nat. Mater.* **2007**, *6*, 183–191.
(17) Jiao, L. Y.; Zhang, L.; Wang, X. R.; Diankov, G.; Dai, H. J. *Nature* **2009**, *458*, 877–880.
(18) Kosynkin, D. V.; Higginbotham, A. L.; Sinitskii, A.; Lomeda, J. R.; Dimiev, A.; Price, B. K.; Tour, J. M. *Nature* **2009**, *458*, 872–875.
(19) Li, X. L.; Wang, X. R.; Zhang, L.; Lee, S. W.; Dai, H. J. *Science* **2008**, *319*, 1229–1232.
(20) Jin, C. H.; Lan, H. P.; Peng, L. M.; Suenaga, K.; Iijima, S. *Phys. Rev. Lett.* **2009**, *102*, 205501.
(21) Li, Q.; Newberg, J. T.; Walter, E. C.; Hemminger, J. C.; Penner, R. M. *Nano Lett.* **2004**, *4*, 277–281.
(22) Li, Q.; Walter, E. C.; van der Veer, W. E.; Murray, B. J.; Newberg, J. T.; Bohannan, E. W.; Switzer, J. A.; Hemminger, J. C.; Penner, R. M. *J. Phys. Chem. B* **2005**, *109*, 3169–3182.
(23) Remskar, M.; Skraba, Z.; Regula, M.; Ballif, C.; Sanjines, R.; Levy, F. *Adv. Mater.* **1998**, *10*, 246–249.
(24) Smith, B. W.; Monthioux, M.; Luzzi, D. E. *Nature* **1998**, *396*, 323–324.
(25) Li, H. J.; Feng, L.; Guan, L. H.; Shi, Z. J.; Gu, Z. N. *Solid State Commun.* **2004**, *132*, 219–224.
(26) Qiu, H. X.; Shi, Z. J.; Guan, L. H.; You, L. P.; Gao, M.; Zhang, S. L.; Qiu, J. S.; Gu, Z. N. *Carbon* **2006**, *44*, 516–521.

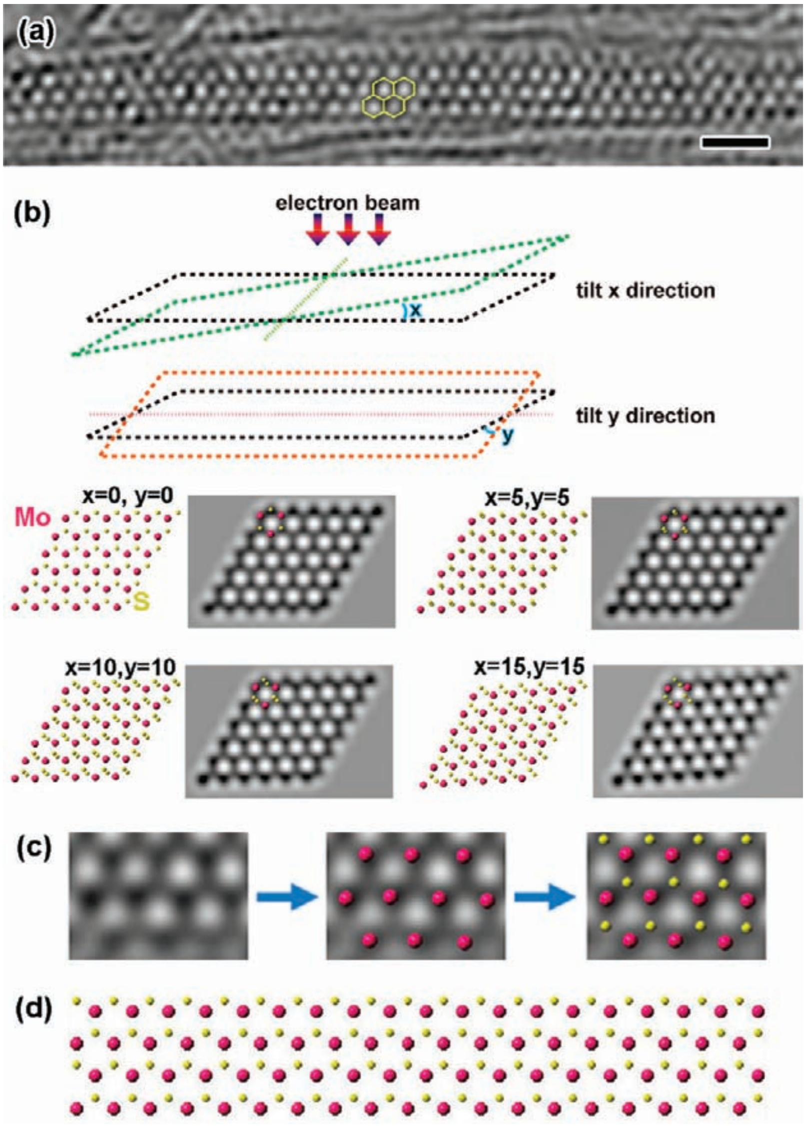

Figure 2. (a) HR-TEM image of a single-layer MoS_2NR encapsulated in a SWCNT. This MoS_2NR is identified as a 4-$ZMoS_2NR$. The scale bar represents 1 nm. (b) HR-TEM simulations and structural models of a single layer of MoS_2 at four different tilt angles. (c) Enlarged view of the image in (a). The dark spots are assigned to Mo atoms. The theoretical distance between the adjacent Mo atoms of MoS_2NR is 0.316 nm. The measured distance between the adjacent dark dots is 0.31 nm, strongly supporting the identification of MoS_2NR. (d) Schematic model of the MoS_2NR in (a).

filled CNTs were separated from the solution by filtration and washing with deionized water. The sample was dried and then heated at 800 °C under a H_2S/H_2 atmosphere for 2 h to generate MoS_2.

A JEM-2010F transmission electron microscope equipped with a CEOS postspecimen spherical aberration corrector (C_s corrector) was operated at 120 kV for high-resolution transmission electron microscopy (HR-TEM) imaging. A Gatan 894 charge-coupled device (CCD) camera was used for digital recording of the HR-TEM images. A sequence of HR-TEM images (20 frames) was recorded, with a 0.5 s exposure time for each. After drift compensation, some frames could be superimposed to increase the signal-to-noise (SN) ratio for display. C_s was set in the range 0.5−2 μm, and the HR-TEM images were recorded under slightly underfocused conditions in order to enhance the contrast of the encapsulated materials with respect to the graphene network of CNTs; this ensured that the contrast of the CNTs could be minimized by fabricating a desirable contrast transfer function (CTF). Image simulations were carried out using the *MacTempas* software package. A JEM-ARM200F microscope incorporating a CEOS prespecimen spherical aberration corrector was operated at 80 kV for energy-dispersive X-ray (EDX) and electron-energy-loss spectroscopy (EELS) analyses. The electron probe, after its aberrations were corrected, featured a current density level that was an order of magnitude higher than that of conventional transmission electron microscopes and was capable of atomic-level analysis. Raman measurements were performed using a JASCO NR2100 system with an excitation wavelength of 514.5 nm. The spectra were obtained by integrating for 180 s for two cycles. A silicon wafer was used to calibrate the spectra.

Results and Discussion

HR-TEM images showed that nanoribbons are formed inside the SWCNTs and DWCNTs with lengths from tens of nanometers to >100 nm (see Figures S1 and S2 in the Supporting Information). Figure 1a shows an annular dark-field image of two single-layer MoS_2NRs, and the lower one has a twisted structure. EDX analysis was performed on the area denoted by the rectangle in Figure 1b. The existence of Mo was easily confirmed from the EDX spectrum; however, the S K peak and Mo L peak overlapped and could not be discriminated. Therefore, EELS analysis (Figure 1c) was also carried out on the same area. The L edge of S atoms located at 165 eV revealed

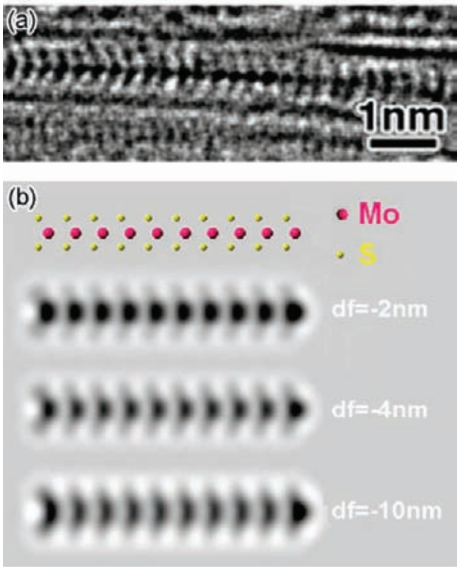

Figure 3. (a) HR-TEM image of a single-layer MoS_2NR parallel to the incident electron beam. (b) Schematic model and simulated images of a single-layer MoS_2NR under three different defocus conditions.

the existence of S atoms. Figure 1d shows the Raman spectra obtained from the MoS_2NR@SWCNT and MoS_2NR@DWCNT nanoburrito samples, together with the reference spectrum of SWCNTs. Two Raman peaks at ∼383 and ∼409 cm^{-1}, corresponding to the MoS_2 E^1_{2g} and A_{1g} modes, respectively, can be seen.[22,27] Furthermore, the line shape of the radial breathing mode (RBM) of MoS_2NR@SWCNTs at ∼160 cm^{-1} differs from that of the original SWCNTs. Such changes in the RBM line shape have frequently been observed for molecule-encapsulated SWCNTs.[28,29] On the basis of the HR-TEM observations without byproducts, almost all of the starting $H_3PMo_{12}O_{40}$ was transformed into nanoribbons, and SWCNTs have a higher nanoribbon filling ratio than DWCNTs.

When SWCNTs with diameters (d) of 1.3−1.6 nm were used as templates, single-layer MoS_2NRs were produced. The widths (w) of the single-layer MoS_2NRs inside the SWCNTs were less than 1.3−1.6 nm. Figure 2a shows a typical HR-TEM image of a single-layer MoS_2NR encapsulated in a SWCNT with the incident electron beam nearly perpendicular to the MoS_2 basal plane. The hexagonal pattern, uniform width, and smooth edge can be clearly seen, and the MoS_2NR is unambiguously assigned as a zigzag-edged nanoribbon. In contrast to GNRs, for which both zigzag and armchair edges have been observed,[30] *all of the plane views of MoS_2NRs in our sample showed zigzag edges*. The projection of a single-layer MoS_2NR under the electron beam depends on the relative orientation. Simulations of the projection of a single-layer MoS_2 as a function of tilt angle are shown in Figure 2b and Figure S3 in the Supporting Information. The contrasts of Mo and S atoms are very similar when the tilting angle is smaller than 5°. When the MoS_2 layer is tilted to a larger degree, the contrast of Mo atoms is darker than that of S atoms, allowing these two kinds of atoms to be discriminated. Consequently, the darker spots in Figure 2a could be ascribed to Mo atoms, which enabled us to assign the S atoms and describe the atomic structure of the MoS_2NR. The lower edge of the nanoribbon is the Mo edge and the upper one the S edge, and there are four Mo atom layers along its width axis (as shown schematically in Figure 2d). Following the convention for GNRs,[31] we use the labels N-ZMoS_2NR and N-AMoS_2NR to denote zigzag and armchair MoS_2NRs, respectively, with N zigzag chains (dimer lines) across the ribbon width. The MoS_2NR in Figure 2a can be unambiguously identified as a 4-ZMoS_2NR. The width of this nanoribbon was determined to be $w = 1.0$ nm, which is the smallest width available for the MoS_2NRs in our sample and approaches the width limit of a MoS_2NR.

In our experiment, MoS_2NRs parallel to the incident electron beam are often observed, and one such HR-TEM image is shown in Figure 3a. The defocus amounts from the left side to the right side are different because of the inclination of the CNTs with respect to the electron beam. This was further corroborated by HR-TEM simulations of a MoS_2NR under a series of defocus conditions (Figure 3b). The dark spots in the center of the fishbonelike projection correspond to Mo atoms, while the two sides of the fishbone with less gray scale correspond to S atoms. This demonstrates that the MoS_2NR in Figure 3a consists of only one layer of Mo atoms.

The widths of the MoS_2NRs synthesized in DWCNTs are $w < 1.5-4.0$ nm on the basis of the inner tube diameters ($d_{\text{inner}} = 1.5-4.0$ nm) for the DWCNTs. Only double-layer and triple-layer MoS_2NRs were observed inside DWCNTs, although a large DWCNT with $d_{\text{inner}} = 4.0$ nm has enough space to accommodate a four-layer MoS_2NR. Figure 4a shows a HR-TEM image of a double-layer MoS_2NR encapsulated in a DWCNT in which the basal plane of the MoS_2NR is parallel to the incident electron beam. Each MoS_2 layer exhibits a sandwich structure, i.e., the central deep dark line corresponds to the Mo layer and the other two shallow dark lines beneath and above the Mo layer correspond to the S layers. The interlayer distance in the MoS_2NR is 0.62 nm, in agreement with that in the hexagonal phase of MoS_2 (0.618 nm). Figure 4b is a schematic model of the double-layer MoS_2NR encapsulated in the DWCNT of Figure 4a. Figure 4c shows an HR-TEM image of a MoS_2NR inside a DWCNT in which the basal plane of the MoS_2NR is perpendicular to the incident electron beam. The right part of this nanoribbon displays a hexagonal pattern and can be identified as 13-ZMoS_2NR. Figure 4d is a schematic model of the 13-ZMoS_2NR encapsulated in the DWCNT of Figure 4c. An HR-TEM image of a triple-layer MoS_2NR encapsulated in a DWCNT is available in Figure S4 in the Supporting Information.

Careful HR-TEM examinations of MoS_2NR@SWCNTs and MoS_2NR@DWCNTs revealed that the encapsulated MoS_2NRs can be seriously twisted, and both radial shrinkage and expansion of the host CNTs were observed at a fixed electron beam incidence angle (Figure S5 in the Supporting Information). The cross section of the CNT expands in the direction of the nanoribbon plane and simultaneously shrinks in the perpendicular direction. The radial deformations of the SWCNT and

---

(27) Frey, G. L.; Tenne, R.; Matthews, M. J.; Dresselhaus, M. S.; Dresselhaus, G. *Phys. Rev. B* **1999**, *60*, 2883–2892.

(28) Yanagi, K.; Iakoubovskii, K.; Matsui, H.; Matsuzaki, H.; Okamoto, H.; Miyata, Y.; Maniwa, Y.; Kazaoui, S.; Minami, N.; Kataura, H. *J. Am. Chem. Soc.* **2007**, *129*, 4992–4997.

(29) Joung, S. K.; Okazaki, T.; Kishi, N.; Okada, S.; Bandow, S.; Iijima, S. *Phys. Rev. Lett.* **2009**, *103*, 027403.

(30) Jia, X. T.; Hofmann, M.; Meunier, V.; Sumpter, B. G.; Campos-Delgado, J.; Romo-Herrera, J. M.; Son, H. B.; Hsieh, Y. P.; Reina, A.; Kong, J.; Terrones, M.; Dresselhaus, M. S. *Science* **2009**, *323*, 1701–1705.

(31) Son, Y. W.; Cohen, M. L.; Louie, S. G. *Phys. Rev. Lett.* **2006**, *97*, 216803.

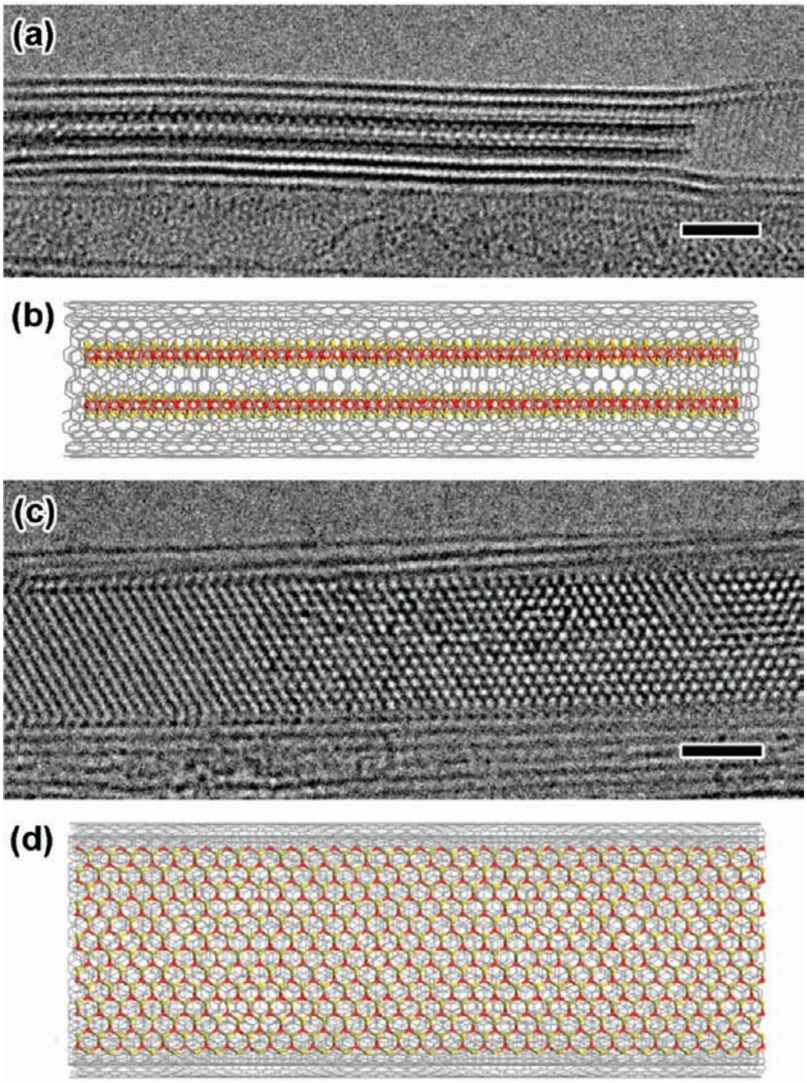

Figure 4. (a) HR-TEM image and (b) schematic model of a double-layer MoS_2NR encapsulated in a DWCNT. The basal plane of the MoS_2NR is parallel to the incident electron beam. (c) HR-TEM image and (d) schematic model of a 13-$ZMoS_2NR$ with $w \approx 3.3$ nm encapsulated in a DWCNT. The basal plane of the MoS_2NR is nearly perpendicular to the incident electron beam. In the models, red balls represent Mo, yellow balls S, and gray balls C. Scale bars in the HR-TEM images represent 2 nm.

DWCNT shown in Figure S5 are 45 and 22%, respectively, as measured by the aspect ratio. The radial deformation is ascribed to the strong interaction between the edge of the MoS_2NRs and the inner wall of the CNTs and would significantly modify the electronic properties of the CNTs (as shown by the DFT calculations discussed below). Previous reports have shown that encapsulation of CoI_2[32] or I[33] chains into SWCNTs also causes an appreciable radial deformation of the SWCNTs.

In order to identify the details of the edge and explain the dominance of the zigzag edge over the armchair edge, we perform intensive DFT calculations on free-standing 1 nm wide 4-$ZMoS_2NRs$ and 7-$AMoS_2NRs$. In our 4-$ZMoS_2NR$ model, S coverages of 0, 50, and 100% for the Mo edge were considered, and 100% S coverage with and without H passivation were considered for the S edge. We use the notation $Mo_{(p\%S)}$-$S_{(q\%H)}$ to indicate the edge configuration of the 4-$ZMoS_2NR$ with a Mo edge saturated by p% S and a S edge saturated by q% H. In contrast, in our 7-$AMoS_2NR$ model, complete bareness (0% H) and full H passivation (100% H) of the edge S atoms were considered. The ultrasoft pseudopotential[34] plane-wave basis set as implemented in the CASTEP[35] package with a cutoff energy of 290 eV was used. A $1 \times 1 \times 49$ Monkhorst−Pack[36] k-point grid was used for the integration of the first Brillouin zone. Each geometry optimization was carried out until the maximum force was less than 0.03 eV/Å. Spin-polarized quantum transport calculations were performed using the ATK2008.10 code,[37,38] which is based on DFT coupled with the nonequilibrium Green's function (NEGF) method. In the composite models, a double numerical (DN) atomic-orbital basis set and effective core

---

(32) Philp, E.; Sloan, J.; Kirkland, A. I.; Meyer, R. R.; Friedrichs, S.; Hutchison, J. L.; Green, M. L. H. *Nat. Mater.* **2003**, *2*, 788–791.

(33) Guan, L. H.; Suenaga, K.; Shi, Z. J.; Gu, Z. N.; Iijima, S. *Nano Lett.* **2007**, *7*, 1532–1535.

(34) Vanderbilt, D. *Phys. Rev. B* **1990**, *41*, 7892–7895.

(35) Milman, V.; Winkler, B.; White, J. A.; Pickard, C. J.; Payne, M. C.; Akhmatskaya, E. V.; Nobes, R. H. *Int. J. Quantum Chem.* **2000**, *77*, 895–910.

(36) Monkhorst, H. J.; Pack, J. D. *Phys. Rev. B* **1976**, *13*, 5188–5192.

(37) Brandbyge, M.; Mozos, J. L.; Ordejon, P.; Taylor, J.; Stokbro, K. *Phys. Rev. B* **2002**, *65*, 165401.

(38) Taylor, J.; Guo, H.; Wang, J. *Phys. Rev. B* **2001**, *63*, 245407.

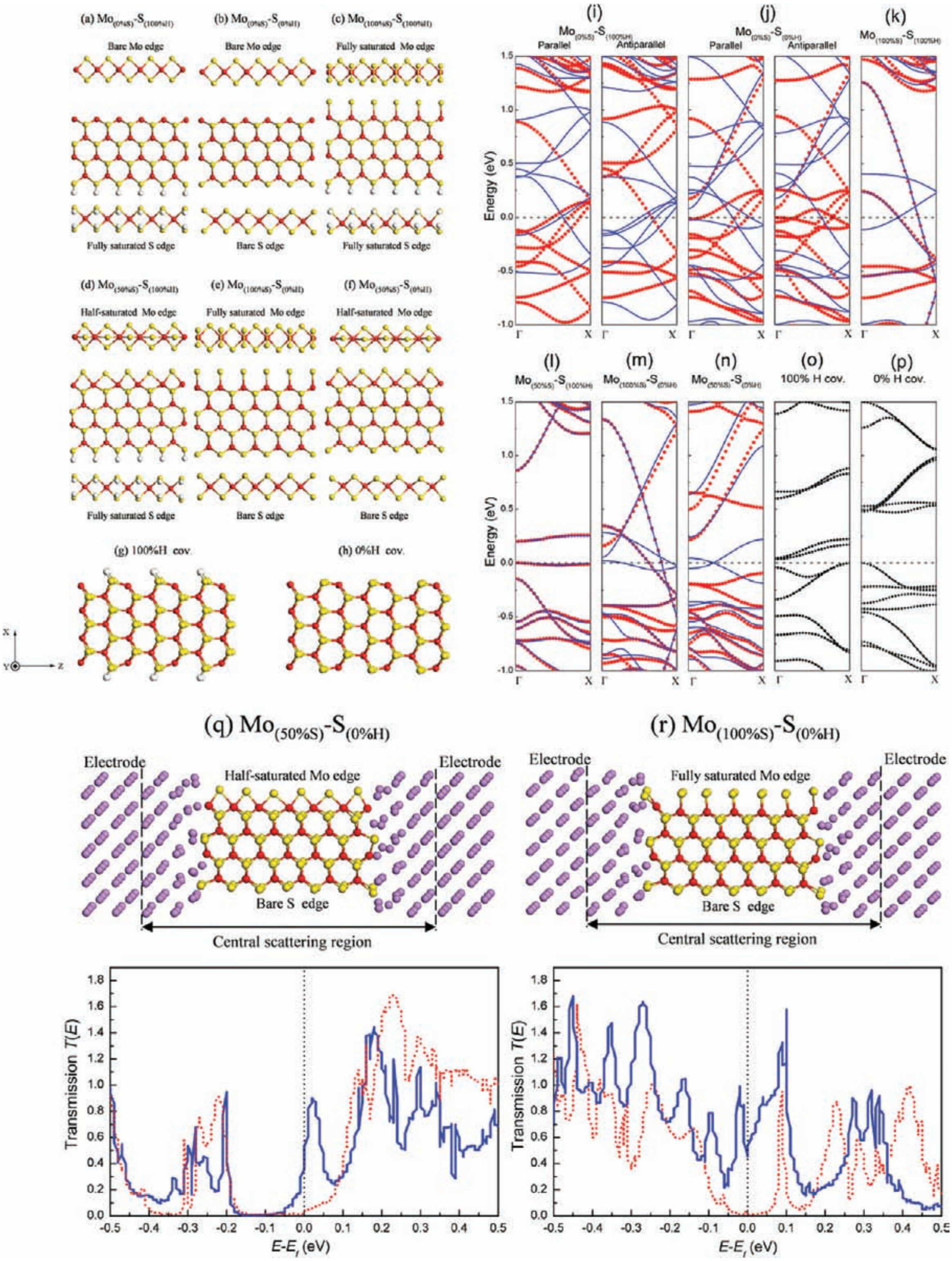

Figure 5. (a−h) Optimized structures of the (a−f) 4-ZMoS$_2$NRs (top and side views) and (g, h) 7-AMoS$_2$NRs. The MoS$_2$NRs are extended along the *z* direction. (i−n) Spin-polarized band structures arranged in order of descending δG of the 4-ZMoS$_2$NRs and (o, p) non-spin-polarized band structures of the 7-AMoS$_2$NRs. (q, r) Optimized two-probe models and transmission spectra for the truncated 4-ZMoS$_2$NRs using Li(100) surfaces as electrodes. The red dotted and blue solid lines represent the spin-up and spin-down states, respectively. The Fermi level is set to zero. Red balls, Mo; yellow balls, S; white balls, H; purple balls, Li.

potentials as implemented in the DMol^3 package[39] were used. Three *k* points were applied in the optimization procedure. The generalized gradient approximation (GGA) in the Perdew−Burke−Ernzerhof (PBE) form[40] was chosen as the exchange-correlation functional in all of the calculations.

The optimized structures of the MoS$_2$NRs are shown in Figure 5a−h, and the features are described in the Supporting Information. Following previous work,[41−43] we define the

---

(39) Delley, B. *J. Chem. Phys.* **1990**, *92*, 508–517.

Table 1. Ground-State Per-Atom Gibbs Free Energy (δG) of Formation, Energy Difference between the Magnetic Ground State and the Nonmagnetic State (ΔE), Electronic Type, Spin Coupling between the Two Edges, Total Magnetic Moment (M_{tot}), and Spin Polarization (ξ) of the 1 nm Wide MoS_2NRs

	4-$ZMoS_2$NRs								7-$AMoS_2$NRs	
	$Mo_{(0\%S)}$- $S_{(100\%H)}$		$Mo_{(0\%S)}$-$S_{(0\%H)}$		$Mo_{(100\%S)}$-$S_{(100\%H)}$	$Mo_{(50\%S)}$-$S_{(100\%H)}$	$Mo_{(100\%S)}$-$S_{(0\%H)}$	$Mo_{(50\%S)}$-$S_{(0\%H)}$	100% H coverage	0% H coverage
δG (eV)	−0.50		−0.53		−0.59	−0.62	−0.63	−0.66	−0.45	−0.52
ΔE (meV)	−197[a]		−110[a]		−103	−107	−81	−156	—[b]	—[b]
electronic type	*M*[c]		*M*		*M*	*S*[d]	*M*	*HM*[e]	*SM*[f]	*S*
edge spin coupling	*P*[g]	*A*[h]	*P*	*A*	—[i]	—[i]	—[i]	*A*	—	—
M_{tot} (μ_B)	4.12	−1.36	3.24	1.12	1.52	0.00	1.20	0.00	—	—
ξ (%)	—		—		—	—	93	89	—	—

[a] The parallel and antiparallel spin-coupling states between the two edges are degenerate in total energy. [b] The ground state is nonmagnetic. [c] *M*: metallic. [d] *S*: semiconducting. [e] *HM*: half-metallic. [f] *SM*: semimetallic. [g] *P*: parallel. [h] *A*: antiparallel. [i] One edge is nonmagnetic.

per-atom Gibbs free energy of formation (δG) for the MoS_2NRs as

$$\delta G = E_{\text{ribbon}} + n_{\text{Mo}}\mu_{\text{Mo}} + n_S\mu_S + n_H\mu_H \tag{1}$$

where $-E_{\text{ribbon}}$ represents the cohesive energy per atom of the MoS_2NRs, n_{Mo}, n_S, and n_H are the mole fractions of Mo, S, and H atoms, respectively, for a given structure, and μ_{Mo}, μ_S, and μ_H are the per-atom chemical potentials of Mo, S, and H, respectively, at a given state. We chose μ_{Mo}, μ_S, and μ_H as the binding energies per atom of bulk Mo, the crown-shaped S_8 molecule, and the H_2 molecule, respectively. The calculated δG values are given in Table 1. In general, the 4-$ZMoS_2$NRs are more stable than the 7-$AMoS_2$NRs. This theoretical relative stability of the two types of MoS_2NRs in the free-standing state is consistent with the observed one in the confined state. The relative stability of the 4-$ZMoS_2$NRs ascends in the following order: $Mo_{(0\%S)}$-$S_{(100\%H)}$ < $Mo_{(0\%S)}$-$S_{(0\%H)}$ < $Mo_{(100\%S)}$-$S_{(100\%H)}$ < $Mo_{(50\%S)}$-$S_{(100\%H)}$ < $Mo_{(100\%S)}$-$S_{(0\%H)}$ < $Mo_{(50\%S)}$-$S_{(0\%H)}$. The most stable 4-$ZMoS_2$NR has a Mo edge half-saturated with S atoms and a H-free S edge.

All of the checked 4-$ZMoS_2$NRs turned out to be magnetic (see Table 1), while the 7-$AMoS_2$NRs were nonmagnetic. The spin distributions of the 4-$ZMoS_2$NRs are provided in Figure S6 in the Supporting Information. A very recent DFT calculation by Zhou et al.[44] also reported a magnetic ground state for $ZMoS_2$NRs with bare Mo and S edges. The band structures for the MoS_2NRs are presented in Figure 5i−p. The 4-$ZMoS_2$NRs with edge configurations labeled as $Mo_{(0\%S)}$-$S_{(100\%H)}$, $Mo_{(0\%S)}$-$S_{(0\%H)}$, $Mo_{(100\%S)}$-$S_{(100\%H)}$, and $Mo_{(100\%S)}$-$S_{(0\%H)}$ were metallic, regardless the type of spin coupling between the two edges (Figure 5i−k,m). Zhou et al.'s DFT calculation also obtained a metallic ground state for the $ZMoS_2$NRs with bare and ferromagnetically coupled Mo and S edges.[44] The 4-$ZMoS_2$NR with the $Mo_{(50\%S)}$-$S_{(100\%H)}$ edge configuration was nearly a spin-degenerate p-type semiconductor with a direct band gap of 1.01 eV (Figure 5l). Remarkably, the 4-$ZMoS_2$NR with the $Mo_{(50\%S)}$-$S_{(0\%H)}$ edge configuration was half-metallic, with two metallic bands across the Fermi level (E_f) in one spin channel and an indirect band gap of 0.50 eV in the other spin channel (Figure 5n). The orbital wave functions of the two metallic states of the half-metallic 4-$ZMoS_2$NR are chiefly localized on the Mo and S edge (see Figure S7 in the Supporting Information). Hence, the spin current travels along the two edges of this nanoribbon. Because this structure has the lowest δG, half-metallicity in MoS_2NRs has a remarkable advantage over GNRs, where harsh generation conditions such as a large transverse in-plane external electric field,[45] different functionalizations on the two edges,[46] or rolling into nanoscrolls[47] are required. We performed transport calculations for two 1.9 nm long truncated 4-$ZMoS_2$NRs with $Mo_{(50\%S)}$-$S_{(0\%H)}$ (half-metallic) and $Mo_{(100\%S)}$-$S_{(0\%H)}$ edge configurations. The latter had the second-lowest δG along with four and two bands across E_f in the spin-down and spin-up channels, respectively. Two-probe models with the truncated 4-$ZMoS_2$NRs chemically bonded to quasi-one-dimensional Li electrodes were built (Figure 5q,r). We define the spin polarization (ξ) of the electron current as

$$\xi = \left|\frac{T^{\text{down}} - T^{\text{up}}}{T^{\text{down}} + T^{\text{up}}}\right| \tag{2}$$

where T^{down} and T^{up} represent the transmission coefficients of the spin-down and spin-up channels, respectively. The half-metallic 4-$ZMoS_2$NR and the metallic 4-$ZMoS_2$NR with the $Mo_{(100\%S)}$-$S_{(0\%H)}$ edge configuration showed notably large spin polarizations of 89 and 93% at E_f, respectively, suggestive of highly effective spin filters.

We also explored the electronic properties of the MoS_2NR@SWCNT composite. We found that the length of four periods of $ZMoS_2$NR is nearly equal to that of three periods of a zigzag SWCNT. Thus, we constructed a supercell model consisting of a bare 4-$ZMoS_2$NR with four unit cells and a zigzag (16,0) SWCNT with three unit cells. The optimized structures of the 4-$ZMoS_2NR_{Mo_{(0\%S)}\text{-}S_{(0\%H)}}$@(16,0)SWCNT and 4-$ZMoS_2NR_{Mo_{(50\%S)}\text{-}S_{(0\%H)}}$@(16,0)SWCNT nanoburritos are shown in Figures S8a and S9a, respectively, in the Supporting Information. The host (16,0) SWCNTs are severely deformed, with radial deformations of 43 and 58%, respectively, which can be compared with the value of 45% observed in our experiment. The magnetism of the inner 4-$ZMoS_2$NRs is completely quenched by the host (16,0) SWCNT. Experimentally, no magnetism was observed in our MoS_2NR@CNT nanoburrito sample. The 4-$ZMoS_2NR_{Mo_{(0\%S)}\text{-}S_{(0\%H)}}$@(16,0)SWCNT and 4-$ZMoS_2NR_{Mo_{(50\%S)}\text{-}S_{(0\%H)}}$@(16,0)SWCNT are a semimetal and metal (Figures S8b and S9b), respectively, and the corresponding deformed host SWCNTs have direct band gaps of 0.16

---

(40) Perdew, J. P.; Burke, K.; Ernzerhof, M. *Phys. Rev. Lett.* **1996**, *77*, 3865–3868.

(41) Barone, V.; Hod, O.; Scuseria, G. E. *Nano Lett.* **2006**, *6*, 2748–2754.

(42) Chen, R. Y.; Wang, L.; Lai, L.; Lu, J.; Luo, G. F.; Zhou, J.; Gao, Z. X. *J. Nanosci. Nanotechnol.* **2009**, *9*, 1754–1759.

(43) Dumitrica, T.; Hua, M.; Yakobson, B. I. *Phys. Rev. B* **2004**, *70*, 241303.

(44) Li, Y. F.; Zhou, Z.; Zhang, S. B.; Chen, Z. F. *J. Am. Chem. Soc.* **2008**, *130*, 16739–16744.

(45) Son, Y. W.; Cohen, M. L.; Louie, S. G. *Nature* **2006**, *444*, 347–349.

(46) Kan, E. J.; Li, Z. Y.; Yang, J. L.; Hou, J. G. *J. Am. Chem. Soc.* **2008**, *130*, 4224–4228.

(47) Lai, L.; Lu, J.; Wang, L.; Luo, G. L.; Zhou, J.; Qin, R.; Chen, Y.; Li, H.; Gao, Z. X.; Li, G. P.; Mei, W. N.; Maeda, Y.; Akasaka, T.; Sanvito, S. *Nano Res.* **2009**, *2*, 844–850.

eV (Figure S8d) and zero (Figure S9d), respectively, which can be compared with the 0.59 eV direct band gap (Figures S8c and S9c) of the intact host (16,0) SWCNT. The conductivities of the composite 4-ZMoS$_2$NR@(16,0)SWCNT structures are mainly contributed by the inner 4-ZMoS$_2$NRs (Figure S8e and S9e).

Finally, we expect that the synthesis route proposed in this article is extendable to the synthesis of other ultranarrow transition-metal chalcogenide nanoribbons (e.g., WS$_2$, SnS$_2$, VS$_2$, and TiS$_2$) and CNTs. As a first step, we have synthesized ultranarrow WS$_2$ nanoribbons inside CNTs, and the results of that work will be published elsewhere.

Conclusion

We have developed a route for the synthesis of ultranarrow MoS$_2$ nanoribbons with uniform width and smooth edges that employs carbon nanotubes as templates. This route is extendable to the synthesis of other ultranarrow transition-metal chalcogenide nanoribbons. The widths of the MoS$_2$ nanoribbons are in the range of 1−4 nm and the layer numbers are 1−3, depending on the diameter of the carbon nanotubes. Both experiment and theory show than the zigzag-edged MoS$_2$ nanoribbons are generally more stable than the armchair-edged MoS$_2$ ones. The Mo edge of the zigzag-edged MoS$_2$ nanoribbons tends to be half-saturated by S atoms, while the S edge prefers to be bare.

Acknowledgment. This work was supported by the NSFC (Grants 90206048, 20771010, 10774003, 90606023, and 20731160012), the National 973 Project (2006CB932701, 2007AA03Z311, and 2007CB936200, MOST of China), Fundamental Research Funds for the Central Universities, and the Program for New Century Excellent Talents in University of the MOE of China. J.L. thanks Prof. W. N. Mei for helpful discussion. K.S. and Z.L. acknowledge the support by CREST and a Grant-in-Aid from MEXT (19054017), and Z.L. acknowledges the partial support by the Hayashi Memorial Foundation for Female Natural Scientists. Dr. Okunishi (JEOL) and Dr. T. Saito (AIST) are also acknowledged for their kind help with the EDX and Raman measurements, respectively.

Supporting Information Available: Structural character of the optimized MoS$_2$NRs; HR-TEM images of the long single-layer and double-layer MoS$_2$NRs encapsulated in a SWCNT and DWCNT, respectively; HR-TEM simulation of single-layer MoS$_2$NRs at different tilting angles; HR-TEM image and schematic model of a triple-layer MoS$_2$NR encapsulated in a DWCNT; HR-TEM images of twisted single-layer and double-layer MoS$_2$NRs encapsulated in a SWCNT and DWCNT, respectively; spin distributions of the 4-ZMoS$_2$NRs; isosurfaces of the orbital wave functions of the two conduction bands at the Γ point for the 4-ZMoS$_2$NR with the Mo$_{(50\%S)}$-S$_{(0\%H)}$ edge configuration; and the optimized structure, band structure, and density of states of the 4-ZMoS$_2$NR@(16,0)SWCNT composite. This material is available free of charge via the Internet at http://pubs.acs.org.

JA1058026